SUPPORTING INFORMATION

Impact of SnF_2 addition on the chemical and electronic surface structure of $CsSnBr_3$

Claudia Hartmann[1§], Satyajit Gupta[2,3§], Tatyana Bendikov[4], Xeniya Kozina[1], Thomas Kunze[1], Roberto Félix[1], Gary Hodes[2], Regan G. Wilks[1,5], David Cahen[2*], and Marcus Bär[1,5,6,7*]*

[1]*Interface Design, Helmholtz-Zentrum Berlin für Materialien und Energie GmbH (HZB), 14109 Berlin, Germany.*

[2]*Dept. of Materials & Interfaces, Weizmann Institute of Science (WIS), Rehovot, 7610001, Israel.*

[3]*Department of Chemistry, Indian Institute of Technology Bhilai, GEC Campus, Chhattisgarh 492015, India.*

[4]*Chemical Research Support Unit, WIS, Rehovot, 7610001, Israel.*

[5]*Energy Materials In-Situ Laboratory Berlin (EMIL), HZB, 12489 Berlin, Germany.*

[6]*Helmholtz-Institute Erlangen-Nürnberg for Renewable Energy (HI ERN), HZB, 12489 Berlin, Germany.*

[7]*Department of Chemistry and Pharmacy, Friedrich-Alexander-Universität Erlangen-Nürnberg, 91058 Erlangen, Germany.*

[§]*Equal contributions.*

Corresponding Authors

[*]E-mail: gary.hodes@weizmann.ac.il

[*]E-mail: david.cahen@weizmann.ac.il

[*]E-mail: marcus.baer@helmholtz-berlin.de

Experimental Section

Five sample batches of $CsSnBr_3$/c-TiO_2/FTO/glass samples with and without 20 mol% SnF_2 samples were prepared sequentially at the Weizmann Institute of Science (WIS) in Israel according to ref.[1]. Samples were shipped from the WIS after being sealed in an inert atmosphere to minimize exposure to air.

Upon arrival at the HZB, the samples were stored and mounted for measurements in an N_2-filled glovebox directly attached to the lab-based characterization system. Initial surface chemical structure analysis of the samples was done via x-ray photoelectron spectroscopy (XPS), using a Scienta EW4000 electron analyzer[2] (using pass energies of 30 eV) and non-monochromatized Al K_α excitation (1486.58 eV, 300 W) from a PREVAC RS40B1 twin anode x-ray source[3] at the Energy Materials In-Situ Laboratory Berlin (EMIL).[4] The base pressure of the XPS chamber was $< 1 \times 10^{-9}$ mbar.

For comparison purposes, XPS measurements at WIS of similarly prepared samples were carried out. Those measurements were done within a day of preparation. The samples were kept in inert atmosphere after preparation, and transfer to the Kratos AXIS ULTRA system was done through

a N_2-filled glovebox attached to the instrument. The measurements were done with a monochromatized Al K_α x-ray source at 75 W and pass energies ranging between 20 and 80 eV. The instrument is equipped with a hemispherical electron energy analyzer and a delay line detector (DLD). The base pressure in the measuring chamber was $< 1 \times 10^{-9}$ mbar.

Synchrotron-based hard x-ray photoelectron spectroscopy (HAXPES) measurements with an excitation energy of 2003 eV (from here on and in the manuscript referred to as 2 keV for simplicity) were carried out at the HiKE endstation[5] located at HZB's BESSY II KMC-1 beamline.[6] This station is equipped with a Scienta R4000 hemispherical electron energy analyzer. The base pressure of the endstation was $< 1 \times 10^{-8}$ mbar. For the HAXPES measurements significant efforts were made to avoid air-exposure by transferring them into the endstation loadlock using a N_2-purged glovebag. The energy scale for all measurements was calibrated by measuring Au 4f spectra of a clean, electrically grounded Au foil and setting the Au $4f_{7/2}$ binding energy to 84.00 eV.[7]

Curve fit analysis of XPS and HAXPES detail spectra measured at HZB were simultaneously conducted with the Unift 2016 software[8] using Voigt function profiles, keeping the Lorentzian and Gaussian full width at half maximum (FWHM) values fixed for the same core levels, and a Shirley background. The HAXPES shallow core level spin-orbit doublets were fitted with two Voigt profiles with intensity ratios set to obey the $2j+1$ multiplicity rule. The doublet separation was fixed to 1.1 eV for Sn 4d,[9] to 1.05 eV for Br 3d,[10] and to 2.3 eV for Cs 4d.[11] To derive the Cs/Sn and Br/Sn composition ratios the corresponding line intensities were only corrected by respective photoionization cross sections[12,13] (i.e., the similar kinetic energies of the photoelectrons derived from these shallow core levels result in negligible differences in inelastic mean free paths (IMFP) and electron analyzer transmission). For computing the F/Sn ratio the intensities of the XPS Sn 3p

and F 1s were used. Again, the photoemission lines have very similar kinetic energies and so the intensity ratio was only corrected by the corresponding photoionization cross sections.[12,13]

Curve fit analysis of the high-resolution XPS spectra of Cs 3d, F 1s, Sn 3d, and Br 3d measured at WIS were done with the Vision 2.2.10 software, especially developed for the Kratos AXIS ULTRA system.[14] The software includes automatic correction of the raw data for different analyzer transmissions, considering the specific geometry of the instrument, kinetic energies of the photoemission lines, and the pass energies at which measurements were performed.[14] In addition, it includes photoionization cross section correction in terms of considering relative sensitivity factors.[15] Peak fit analyses were based on linear or Shirley background subtraction and application of Gaussian-Lorentzian line profiles. Contrary to the HAXPES and non-monochromatized XPS measurements at HZB, for WIS measurements additional correction for different analyzer transmission is required due to the large kinetic energy spread of the studied photoemission lines. This also requires a correction of the measured photoemission line intensities for any surface contamination layer, as it would impact (attenuate) each line differently [photoelectrons of low kinetic energy (e.g., Cs 3d) will be attenuated stronger than photoelectrons of high kinetic energy (e.g., Br 3d)].

Indeed, a non-negligible quantity of additional C 1s and O 1s intensity ascribed to a surface contamination layer was found on the $CsSnBr_3$/c-TiO_2/FTO/glass and $CsSnBr_3$ + 20 mol% SnF_2/c-TiO_2/FTO/glass samples. Assuming a uniform and homogenous layered structure,[16] we calculated the thickness *d* of this layer according to eq. 1:

$$d = IMFP \cdot \cos\theta \cdot \ln\left(1 + \frac{[C] + [O]}{100 - [C] - [O]}\right) \qquad (1)$$

Surface contamination layer thicknesses of approximately 1.2 and 1.6 nm were obtained for the $CsSnBr_3$/c-TiO_2/FTO/glass and $CsSnBr_3$ + 20 mol% SnF_2/c-TiO_2/FTO/glass samples,

respectively. In eq. 1, IMFP is assumed to be 3.3 nm for the organic layer, neglecting kinetic energy dependencies across the measured energy range.[16-18] θ is the takeoff angle with respect to the surface normal. XPS derived atomic concentrations of carbon and oxygen impurities are given within square brackets. As carbon is the main component of the surface contamination layer, IMFPs for other elements ($IMFP_{el}$) through this layer were corrected vs. C 1s, related to the kinetic energies of these elements ($E_K(el)$), eq. 2,[16,19]

$$IMFP \Big/ IMFP_{el} = \left(\frac{E_K(C\ 1s)}{E_K(el)}\right)^{0.7} \qquad (2)$$

where IMFP = 3.3 nm and $E_K(C\ 1s)$ = (1486.58 – 285) eV ≈ 1202 eV.

Finally, the original photoemission line intensities [$I_{org}(el)$] were corrected for the impact of the surface contamination layer (of a thickness *d*) and the respective IMFP values ($IMFP_{el}$), according to eq. 3, resulting in corrected line intensities [$I_{corr}(el)$]:

$$I_{org}(el) \Big/ I_{corr}(el) = e^{d\left(\frac{1}{IMFP \cdot \cos\theta} - \frac{1}{IMFP_{el} \cdot \cos\theta}\right)} \qquad (3)$$

Since deposition and spectroscopic characterization is mainly performed in different laboratories, part of the work was also to study the reproducibility (e.g., of sample preparation) as well as the impact of environmental (e.g., during transport) and handling (after sample preparation and before characterization) factors on the measured data. Unfortunately, for some of the data the impact of reproducibility, transport, and handling cannot always unambiguously be ascribed to one single reason. However, note that due to the sensitivity of the studied Sn-based perovskites to ambient conditions additional pre- and post-shipping measurements (of x-ray diffraction, etc.) of unencapsulated samples (as are needed for photoemission studies) cannot give meaningful

insights, because the necessary exposure to ambient conditions and to radiation can only add another means by which the sample properties could change.

Scanning electron microscopy (SEM) images (top view) of one $CsSnBr_3$ and $CsSnBr_3$ + 20 mol% SnF_2 sample set on mesoporous TiO_2/compact TiO_2/FTO were taken at WIS using a Leo Ultra 55 scanning electron microscope by measuring secondary electrons with a primary electron beam acceleration voltage of 3 kV using an in-lens detector.

HAXPES shallow core levels

Figure S1 shows HAXPES detail spectra of the shallow core levels energy region of the $CsSnBr_3$ and $CsSnBr_3$ + 20 mol% SnF_2 samples produced by sample batches 1, 3, and 5 [i.e., samples processed without (denoted by A) and with (denoted by B) SnF_2 additive; the batch number is identified by the subscript].

In Figure S1 shallow core levels derived from the signature elements of $CsSnBr_3$ samples, as well as from the elements associated with the c-TiO_2 substrate, can be detected. The peak shapes of the Sn 4d, Br 3d, and Cs 4d spectra indicate the presence of several chemical species (i.e., spectral contributions) for these lines, which is confirmed by curve fit analysis (discussed below). Note that the shallow core level spectra in Figure S1 (and Figure 1) were normalized by subtracting the background around the Fermi level (E_F); the background above E_F arises from scattering of photoemission lines excited by third harmonic excitation of the Si(111) crystal pair of the monochromator of the KMC-1 beamline [i.e., Si(333) ~ 6 keV]. After background subtraction, the spectra were normalized to the Sn 4d line. For the fits used to calculate relative contributions, the

shallow core levels were normalized differently; they were normalized by the background intensity around the Fermi level. For comparison of the ratios between the different shallow core levels of one sample, the contribution from scattering to the background stays constant and thus cancels out.

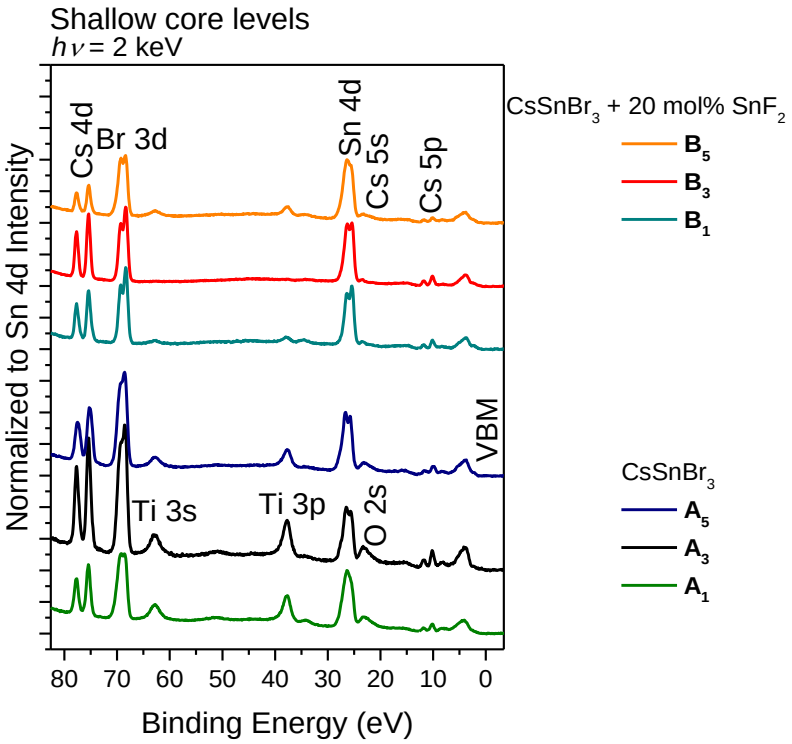

Figure S1. HAXPES spectra of the shallow core level energy region of $CsSnBr_3$ for which no (samples A, "$CsSnBr_3$") and 20 mol% SnF_2 (samples B, "$CsSnBr_3$ + 20 mol% SnF_2") was added to the precursor solution. Sample batches are identified by the subscript. Spectra are shown after background subtraction, normalized to Sn 4d peak height; vertical offsets are added for clarity.

F content variation

Figure S2 shows XPS detail spectra of the F 1s energy region of the investigated $CsSnBr_3$ and $CsSnBr_3$ + 20 mol% SnF_2 samples, measured using Al K_α excitation. The peak detected at binding energy (BE) ~ 685 eV corresponds to the F 1s signal derived from the SnF_2 and can be clearly observed for all $CsSnBr_3$ samples with SnF_2 (i.e., sample set B) measured with Al K_α excitation.[20] No such line is found in the spectra of samples free of SnF_2 (i.e., sample set A). Although the same SnF_2 concentration (i.e., 20 mol %) was incorporated into the precursor solution of all sample batches (for sample set B), the intensity of the F 1s signal varies for the spectra of different sample batches.

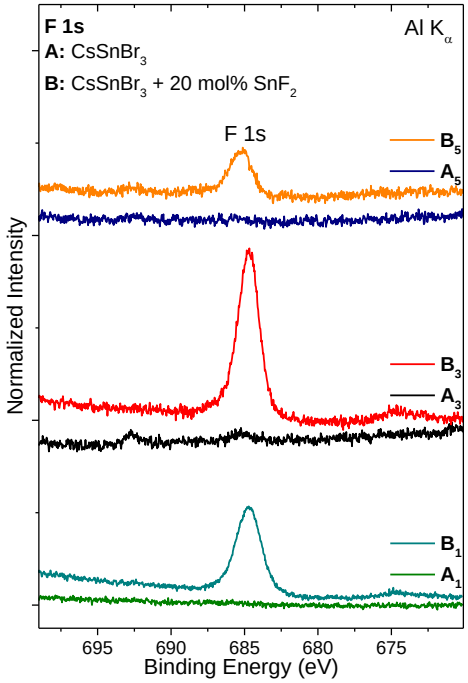

Figure S2. XPS detail spectra of the F 1s energy region of $CsSnBr_3$ (samples A) and $CsSnBr_3$ + 20 mol% SnF_2 (samples B), measured using non-monochromatized Al K_α excitation. Vertical offsets were added for clarity.

Surface morphology

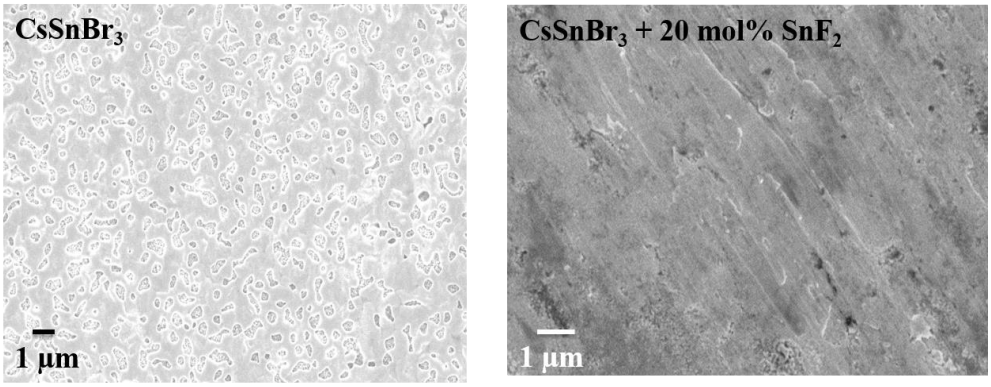

Figure S3. Scanning electron microscopy (SEM) top view images of $CsSnBr_3$ and $CsSnBr_3$ + 20 mol% SnF_2 on mesoporous-TiO_2/compact TiO_2/FTO.

Chemical composition

Figure S4 shows HAXPES detail spectra of the Sn 4d/O 2s/Cs 5s energy region of the $CsSnBr_3$ samples from sample batches 1 and 5, including curve fit analysis and respective residua. (Data on sample batch 3 are presented in the main text.) Satisfactory fits of the spectra are obtained by using two doublet peaks for the Sn 4d related signal, indicating the presence of two Sn species in both sample sets. For the $CsSnBr_3$ samples, shown in Figure S4 (left), the main (i.e., orange area) and secondary (i.e., purple area) Sn $4d_{5/2}$ fit peaks are found at a BE of (25.6 ± 0.1) eV and (26.4 ± 0.1) eV, respectively. Similarly, these fit peaks are located at (25.4 ± 0.1) eV and (26.2 ± 0.1) eV for the $CsSnBr_3$ + 20 mol% SnF_2 samples shown in Figure S4 (right). Based on these results, the main and secondary spectral contributions are ascribed to Sn^{II} and Sn^{IV} species,[9] i.e., a non-oxidized (relative to Sn in $CsSnBr_3$) and an oxidized Sn component, respectively.[21] The O 2s signal (i.e., blue area) is found in the spectra of $CsSnBr_3$ and $CsSnBr_3$ + 20 mol% SnF_2 samples at BE values of (22.1 ± 0.1) eV and (22.0 ± 0.1) eV, respectively, and can be attributed to O from the TiO_2 substrate. Moreover, the signal (i.e., green area) located at a BE of (23.3 ± 0.1) eV for $CsSnBr_3$ and $CsSnBr_3$ + 20 mol% SnF_2 samples is ascribed to Cs 5s states from the perovskite layer.[20] (More

suited approach to characterize the Cs chemical composition of the investigated samples is discussed below, in which the Cs 4d line of the samples is analyzed – see Figure S6.)

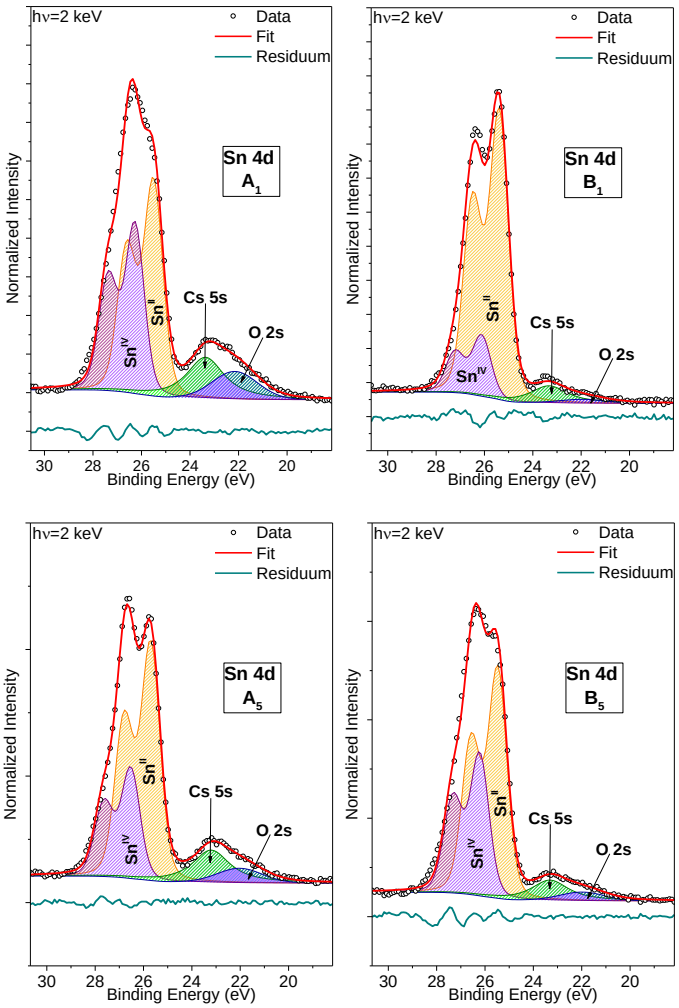

Figure S4. HAXPES detail spectra of the Sn 4d, Cs 5s, and O 2s energy region of $CsSnBr_3$ (sample A, left panel) and $CsSnBr_3$ + 20 mol% SnF_2 (sample B, right panel). Sample batches are identified by the subscript. All spectra are shown with curve fit results including residuals. The spectra were normalized by the background intensity at lower BE around E_F.

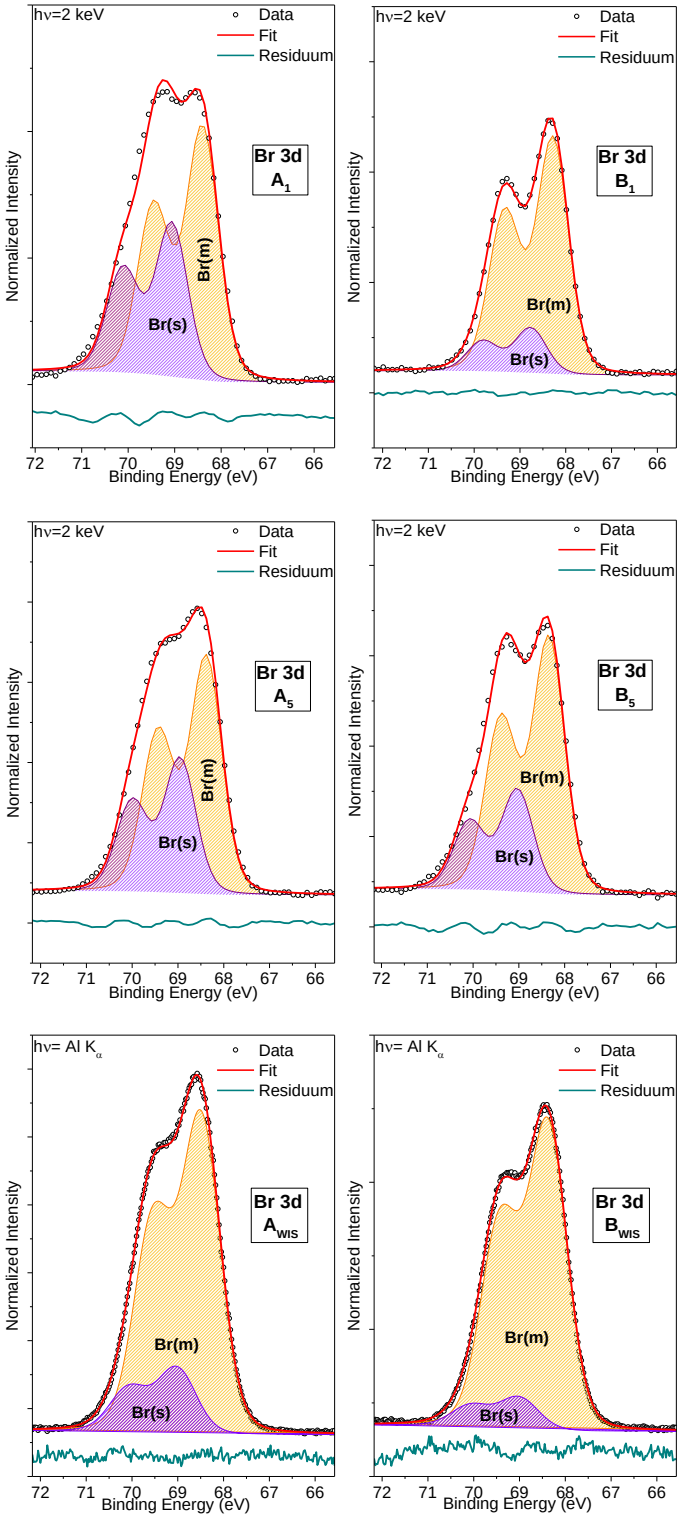

Figure S5. HAXPES detail spectra of the Br 3d energy region of $CsSnBr_3$ (sample A, top and center left panels) and $CsSnBr_3$ + 20 mol% SnF_2 (sample B, top and center right panels) and monochromatized Al K_α XPS detail spectra of the Br 3d energy region of $CsSnBr_3$ (sample A_{WIS}, bottom left panel) and $CsSnBr_3$ + 20 mol% SnF_2 (sample B_{WIS}, bottom right panel). All spectra are shown with curve fit results including residuals. The HAXPES spectra were normalized by the background intensity at lower BE around E_F, while the WIS XPS data are corrected for the transmission function of the analyzer.

Figure S5 shows the HAXPES detail spectra of the Br 3d energy region of the $CsSnBr_3$ samples from sample batches 1 and 5 measured at HZB and the respective XPS data recorded at WIS, including fit analyses and respective residuals. (Data on sample batch 3 are presented in the main text.) As in the case of the fits to the Sn 4d spectra, satisfactory fits of the Br 3d spectra are obtained when using two doublet peaks, corresponding to the presence of two Br chemical species. There is a notable deviation between fit and data in the region around 69 eV (in particular for sample A_1), suggesting that the 2-component fit may be too simplistic and that a third bromine species might be present, as suggested in ref.[22].

The main HAXPES and XPS Br $3d_{5/2}$ fit peak (i.e., maximum of orange component) is found at a BE of (68.4 ± 0.1) eV and (68.3 ± 0.1) eV for the $CsSnBr_3$ and $CsSnBr_3$ + 20 mol% SnF_2 sample sets, respectively, which is attributed to Br-Cs chemical bond environment (e.g., $CsSnBr_3$). The secondary Br $3d_{5/2}$ fit peak (i.e., maximum of purple component) is located at BE of (69.0 ± 0.1) eV and (68.9 ± 0.1) eV for the $CsSnBr_3$ and $CsSnBr_3$ + 20 mol% SnF_2 sample sets, respectively, and can be attributed to Br-Sn oxide-derived states.[20,22]

Figure S6 shows HAXPES detail spectra of the Cs 4d energy region of the $CsSnBr_3$ samples from sample batches 1 and 5 measured at HZB and Figure S7 shows HAXPES detail spectra of the Cs $3d_{5/2}$ energy region from sample batch 1 measured at HZB and the respective XPS data recorded at WIS, including fit analysis and respective residua. (Data on sample batch 3 are presented in the main text.) As in the case of the previously discussed spectra fits, satisfactory fits of the Cs 4d spectra are obtained when two doublet peaks are used, detecting the presence of two Cs chemical species. In Figure S6, the main Cs $4d_{5/2}$ fit peak (i.e., maximum of orange component) is located at an averaged BE of (75.4 ± 0.1) eV for the $CsSnBr_3$ and $CsSnBr_3$ + 20 mol% SnF_2 samples, which might be attributed to Cs-Br bonds (e.g., $CsSnBr_3$).[20] The Cs $4d_{5/2}$ fit peak of the

secondary contribution (i.e., maximum of purple component) is found at a BE value of (74.9 ± 0.1) eV for the $CsSnBr_3$ samples without and at a BE of (74.8 ± 0.1) with 20 mol% SnF_2. Attributing the secondary Cs species to an "oxide" species (as was done for Sn and Br) is thus not straightforward as oxide-related lines are generally reported (and expected) to be at higher BE values than those of the respective metals (see main text for detailed discussion). However, careful dosing experiments of metallic Cs with oxygen show that the Cs core levels shift to lower BE values, even compared to the Cs lines of metallic Cs.[23,24] Therefore, we speculate that the secondary contribution to the Cs 4d line in our study may also be related to a chemical environment best described by Cs "oxide". However, the attribution of this species to, e.g., CsBr can also not be excluded. However, since the surfaces of the studied samples are very Cs-deficient (see Table S1, below), the presence of unreacted CsBr is unlikely.

The Cs $3d_{5/2}$ peak of sample A_{WIS} probed by XPS at WIS was fitted using two Voigt profiles, again indicating the presence of two Cs species (see Figure S7). The Cs $3d_{5/2}$ high BE fit peak is located at (724.7 ± 0.1) eV for the $CsSnBr_3$, which can be ascribed to Cs-Br bonds (e.g., $CsSnBr_3$),[25] in agreement with the above-discussed assignment of the main Cs 4d component. The low BE contribution to the Cs $3d_{5/2}$ peak is at (724.0 ± 0.1) eV and – similar to the secondary Cs 4d contribution – attributed to an "oxide" species. However, for sample A_{WIS}, the low BE peak is the dominant contribution in contrast to the Cs 4d data shown in Figure S6. We attribute the dominance of the "oxide"-related low BE contribution for sample A_{WIS} to the higher surface sensitivity of the XPS measurements. This is corroborated by the respective HAXPES Cs 3d data for sample set 1, also depicted in Figure S7, which shows lower Cs(s)/Cs(m) ratios.

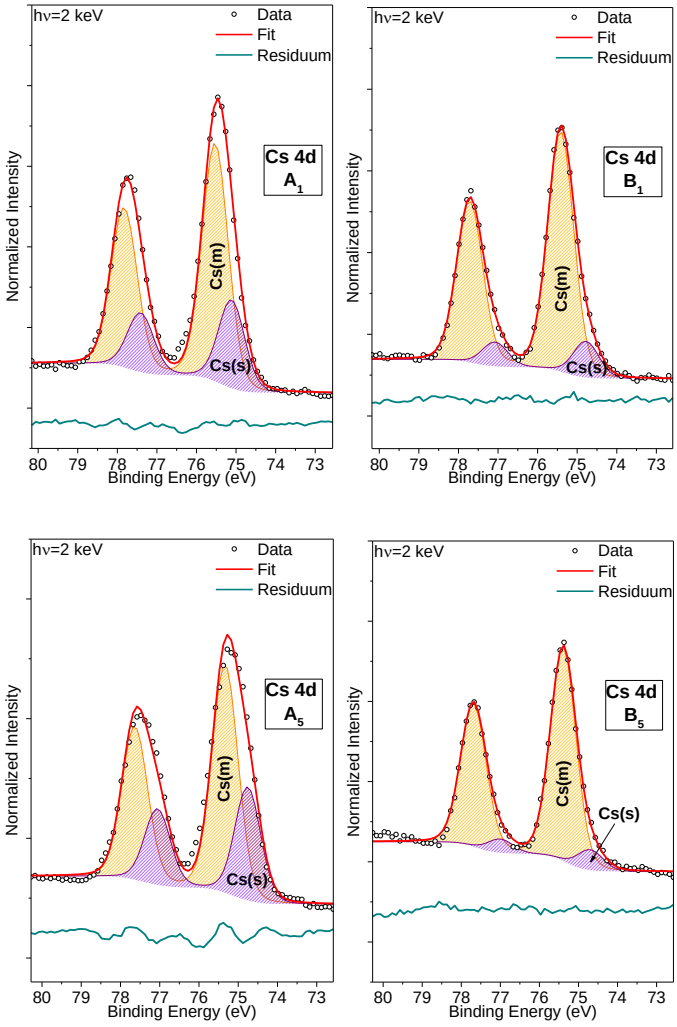

Figure S6. HAXPES detail spectra of the Cs 4d energy region of $CsSnBr_3$ (sample A, left panels) and $CsSnBr_3$ + 20 mol% SnF_2 (sample B, right panels). All spectra are shown with curve fit results including residua. The HAXPES spectra were normalized by the background intensity at lower BE around E_F.

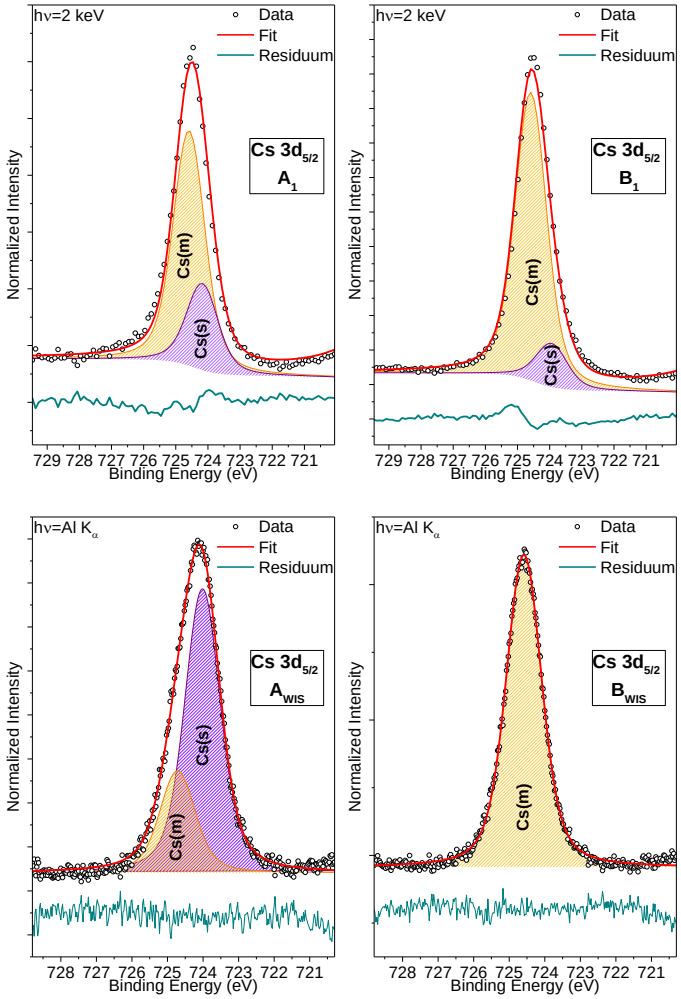

Figure S7. HAXPES detail spectra of the Cs $3d_{5/2}$ energy region of $CsSnBr_3$ (sample A_1, top left panel) and $CsSnBr_3$ + 20 mol% SnF_2 (sample B_1, top right panel) and monochromatized Al K_α XPS detail spectra of the Cs $3d_{5/2}$ energy region of $CsSnBr_3$ (sample A_{WIS}, bottom left panel) and $CsSnBr_3$ + 20 mol% SnF_2 (sample B_{WIS}, bottom right panel) recorded at WIS. All spectra are shown with curve fit results including residua and on a normalized intensity scale.

For the $CsSnBr_3$ + 20 mol% SnF_2 sample, measured at WIS (B_{WIS}), the Cs $3d_{5/2}$ peak can be fit with one contribution, which we ascribe to $CsSnBr_3$, i.e. the addition of SnF_2 to the precursor solution prevents the formation of an (oxide-related) secondary phase. Note that in the related samples measured at HZB (B_1), a small secondary contribution to the Cs $3d_{5/2}$ peak can be identified (see Figure S7). Explanations for this difference could be sample-to-sample variations, the impact of transport from WIS to HZB and/or the longer time between preparation and analysis.

Table S1 shows the chemical composition, derived from the fits of the HAXPES and XPS data recorded at HZB for all three batches compared to the ratios derived from the XPS measurements done at WIS and the nominal expected compositions. Note that the HZB HAXPES and XPS peak areas obtained from the fits were only corrected by the respective photoionization cross sections from ref. [12,13], as the used shallow core levels Sn 4d, Br 3d, Cs 4d / or F 1s and Sn $3p_{3/2}$ lines are close in BE (25 – 80 eV / 685 and 715 eV, respectively) and therefore the impact due to different IMFP and transmission in the analyzer on the quantification is negligible. In contrast, since the WIS XPS derived composition depends also on deep(er) core levels (e.g., Sn $3d_{5/2}$ at a BE of 487 eV, and Cs $3d_{5/2}$ at a BE of 725 eV), their peak areas from the fits were additionally corrected for the transmission function of the analyzer, as provided by the instrument manufacturer, IMFP,[16-19] and the impact of a surface contamination layer. Thus, while the XPS measurements performed at WIS benefit from the short time between sample preparation and characterization, the uncertainty of data quantification is presumably larger compared to the analysis of the shallow core levels measured at HZB.

We find the most significant deviation between individual samples in the F content (see Figure S2). The F/Sn ratio as derived from photoionization-corrected[12,13] areas of F 1s and Sn $3p_{3/2}$ lab-based XPS data measured at HZB varies from 0.05 (for B_5), to 0.13 (for B_1), and to 0.26 (for B_3). Note that the nominal F/Sn ratio is expected to be 0.33 for a 20 mol% Sn excess. Either the F content critically depends on the process parameters (in this case, the observed F/Sn range of 0.05 – 0.26 might indicate the variation inherent to the deposition process) or the samples might lose F during the transport from WIS to HZB or during the time between preparation and analysis. The fact that the F/Sn ratio derived from the XPS measurements performed at WIS is 0.26 (for sample B_{WIS}) and thus right in the F/Sn range based on the HZB XPS data points to inherent variations of

the deposition process as an explanation. Similar to the F/Sn ratio, the Cs/Sn and Br/Sn ratio vary with batch number, but the variation does not seem to correlate to the amount of F present in the sample for sample set B.

Table S1. Compositions calculated from the synchrotron-based HAXPES and lab-based XPS data (measured at HZB and WIS), shown in Figs. S4 - S8, of $CsSnBr_3$ samples deposited without (samples A) and with (samples B) SnF_2 added to the precursor solution, in comparison to the expected nominal composition. For HAXPES the Cs 4d, Br 3d, and Sn 4d lines have been used for quantification; for XPS the Sn 3p, F 1s, Cs 3d, Br 3d, and Sn 3d lines are used. The Cs/Sn, Br/Sn, and F/Sn ratios are derived considering the total intensity (i.e., main + secondary contribution) of the respective photoemission lines. Note that in general the absolute error margin of quantifying photoemission data (which is dominated by the uncertainty of using calculated photoionization cross sections, inelastic mean free paths, and analyzer transmission functions for correction) is estimated to be at least in the order of 30% when stating elemental ratios, but significantly less if relative species ratios of the same element are given. Due to the close proximity if the photoemission lines probed by HAXPES, for quantification the line intensities were only corrected by the corresponding photoionization cross sections and thus the quantification uncertainty is lower than that for the XPS data (see details on HAXPES and XPS quantification above). The sample age (for the HZB measurements, this is the time between receiving the sample and its characterization) at the point of measurement is stated (d – days, m – months). "m" and "s" denote the main and secondary component of the respective photoemission line.

	Cs/Sn	Br/Sn	F/Sn	Sn^{II}/Sn^{IV}	Cs(m)/Cs(s)	Br(m)/Br(s)	Age
Samples A ($CsSnBr_3$)							
Nominal	1	3	-	N/A	N/A	N/A	
1	0.32	1.42	-	1.3	2.7	1.7	8 d
3	0.76	2.65	-	2.0	3.7	2.0	1 m 2 d
5	0.41	1.86	-	2.1	2.0	1.8	2 d
XPS$_{WIS}$	0.15	1.33	-	N/A	0.4	4.9	< 1d
Samples B ($CsSnBr_3$ + 20 mol% SnF_2)							
Nominal	0.83	2.5	0.33	N/A	N/A	N/A	
1	0.33	1.37	0.13	4.7	6.8	5.2	9 d
3	0.35	1.24	0.26	2.9	50.8	4.3	1 m 2-3 d
5	0.15	1.16	0.05	1.6	10.3	2.5	2 d
XPS$_{WIS}$	0.12	0.76	0.26	N/A	N/A	10.0	< 1d

Figure S8 shows HAXPES and XPS (performed at WIS) detail spectra of the Sn 3d energy region of the $CsSnBr_3$ samples and $CsSnBr_3$ + 20 mol% SnF_2 of sample batches 1, 3 and 5 and the corresponding samples characterized at WIS. While there is no indication for the presence/formation of metallic Sn at the surface of the investigated samples [i.e., absence of signal at BE ~ 485 eV, pointed out by the vertical arrows in Figure S8 (top)] in the HAXPES data, a clear spectral feature attributed to Sn^0 can be identified in the XPS data of the $CsSnBr_3$ sample that disappears for the sample that was prepared from a precursor solution that contained 20 mol% SnF_2. Possible explanations for this difference could be related to transport or storage induced modifications of the chemical structure of the $CsSnBr_3$ samples.

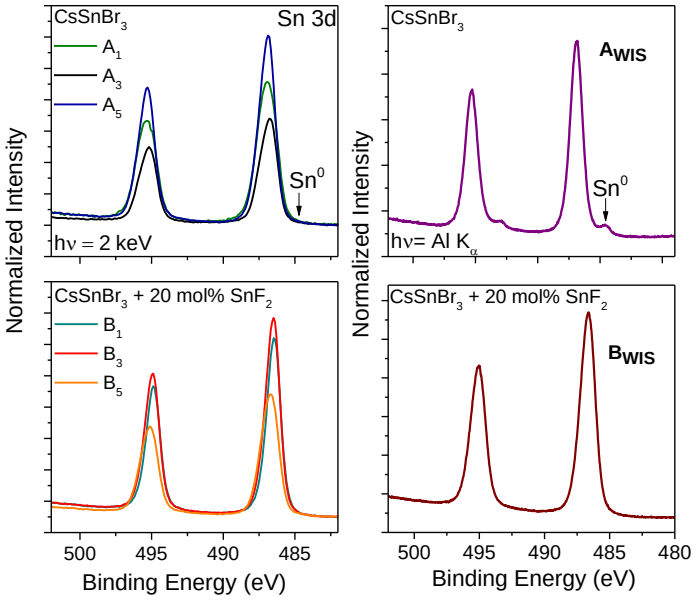

Figure S8. HAXPES (left panels) and XPS (right panels) detail spectra of the Sn 3d energy region of $CsSnBr_3$ samples without (top, denoted A) and with (bottom, denoted B) SnF_2 additive. Sample batches are identified by the subscript.

Effect of SnF_2 on electronic properties

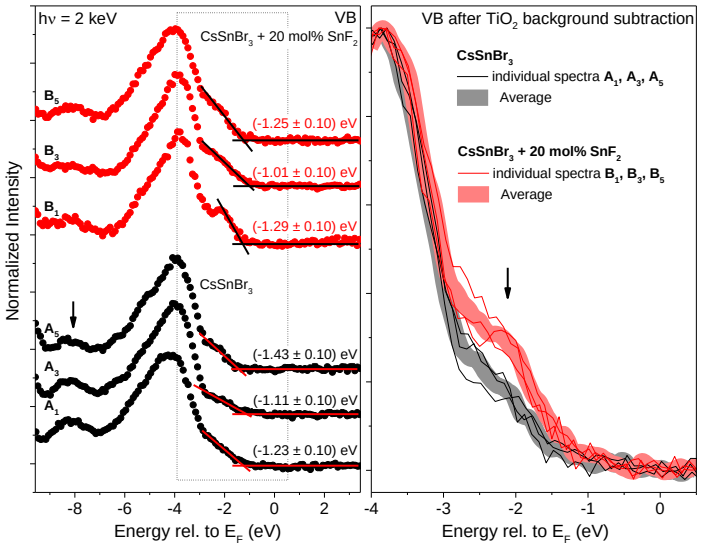

Figure S9. (left) HAXPES detail spectra of the valence band energy region of $CsSnBr_3$ (denoted A) and $CsSnBr_3$ +20 mol% SnF_2 (denoted B), including linear extrapolations of the leading edge of the valence band, used to determine valence band maximum (VBM) values. Sample batches are identified by the subscript. Vertical offsets were added for clarity. (right) Magnified view of the VBM onset for the individual (thin lines) and averaged (thick lines) spectra of the $CsSnBr_3$ and $CsSnBr_3$ + 20 mol% SnF_2 samples, from which the TiO_2 signal was subtracted. All spectra are normalized to maximum intensity.

Figure S9 (left) shows HAXPES detail spectra of the valence band (VB) energy region of the $CsSnBr_3$ samples and $CsSnBr_3$ + 20 mol% SnF_2 for sample batches 1, 3, and 5. The linear extrapolations of the leading edge of the valence band, used to determine the valence band maximum (VBM) values of the investigated samples, are included. The following spectral differences can be noticed between the VB spectra of $CsSnBr_3$ and the $CsSnBr_3$ + 20 mol% SnF_2 samples: the VB spectra of $CsSnBr_3$ samples have a more pronounced BE feature at ~ 8 eV than those of the $CsSnBr_3$ + 20 mol% SnF_2 samples. This feature is ascribed to O 2p-derived density of states (DOS) originating from the TiO_2 substrate, which are visible in the VB spectra due to incomplete coverage of the perovskite.[26] The reduction of this feature observed in the VB spectra of $CsSnBr_3$ + 20 mol% SnF_2 samples shows a similar trend to the observed decrease of the Ti 3p

and O 2s signals in the HAXPES detail spectra of the shallow core level energy region (see Figure S1), an indication of a thicker layer or better coverage of the substrate. Another spectral difference is found in the feature ~ 2 eV from the E_F, which seems to be enhanced for $CsSnBr_3$ + 20 mol% SnF_2 samples. This change can be better seen in Figure S9 (right), which shows a magnified view of the individual and averaged VB spectra (with corresponding substrate signal subtractions[a]) of the three (discussed) batches of $CsSnBr_3$ and $CsSnBr_3$ + 20 mol% SnF_2 samples. According to the literature,[27] this (E_F-2 eV) feature is dominated by Sn 5*s*-derived states and is influenced by changes in the oxidation state of Sn.[9,28] In our case, an increase of Sn 5*s*-derived DOS occurs when reducing the Sn oxidation (i.e., less Sn^{IV} states), which in turn can be related to the SnF_2 treatment.

[a]The substrate signal was treated by subtracting a scaled TiO_2 VB spectrum from all the VB spectra of sample sets A and B, normalized to the background. The TiO_2 VB spectrum was scaled to the O 2p DOS feature at 8 eV of the halide perovskite spectra.

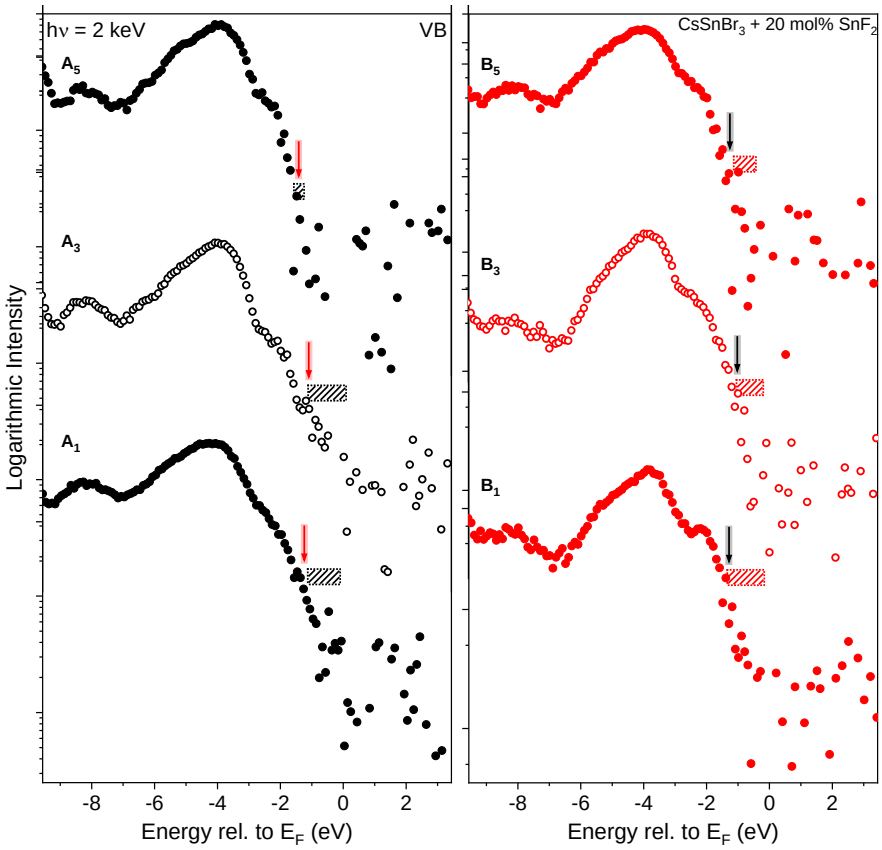

Figure S10. HAXPES detail spectra of the valence band energy region of the $CsSnBr_3$ (denoted A) and $CsSnBr_3$ +20 mol% SnF_2 (denoted B) samples shown on a semi-log scale. Sample batches are identified by the subscript. Vertical offsets were added for clarity. The positions of the VBM values determined from the linear extrapolation shown in Figure S9 are indicated as arrows (the respective shadow indicates the experimental uncertainty). The hatched boxes give the VBM range if the data on a semi-log scale is used for determination.

Figure S10 shows the valence band spectra of sample sets A and B on a semi-logarithmic scale as proposed in ref. [29]. Due to low total photoionization cross section for the VB-derived states when probed with hard x-rays and the background signal relating to higher order excitations from the beamline, the noise floor above VBM is significantly higher than that of UPS measurements. Determining the VBM by semi-log extrapolation of the leading edge to the background, thus, becomes less straightforward and more error prone compared to evaluating the spectra on a linear scale. However, the VBM values derived on a linear scale – while always being on the far side with respect to the distance to E_F – mainly coincide within the experimental uncertainty with the

clear intensity drop of the HAXPES data on a semi-logarithmic scale; thus, we conclude that in our case a semi-log approach does not lead to significantly different VBM values. An explanation for this difference between HAXPES and UPS could be the higher HAXPES sensitivity to s-derived states than the UPS one, and the fact the top of the VB in $CsSnBr_3$ is formed by states having a strong Sn 5*s* character. Generally photoionization cross sections increase when the excitation energy approaches the binding energy of the particular photoemission line (i.e., the total photoionization cross section of the VB states increases for decreasing excitation energies).[12,13] However, in the case considered here (Sn 5*s*-derived states that form the VB onset) employing higher (hard x-ray) excitation energies has the benefit that the photoionization cross section for *s*-derived states decreases significantly less than that for *p*- or *d*-derived states.[12,13] This results in an effective amplification of the spectral intensity of *s*-derived states in the HAXPES spectrum. We speculate that this fact together with the higher DOS at the top of the VB[30] removes the advantage of the semi-log approach over the linear one, when probing the VBM of $CsSnBr_3$ by HAXPES.

REFERENCES

(1) Gupta, S.; Bendikov, T.; Hodes, G.; Cahen, D. $CsSnBr_3$, A Lead-Free Halide Perovskite for Long-Term Solar Cell Application: Insights on SnF_2 Addition. *ACS Energy Letters* **2016**, *1*, 1028–1033.

(2) Scienta Omicron, "Electron Spectrometers," 2017. [Online]. Available: http://www.scientaomicron.com/en/products/electron-spectrometer.

(3) PREVAC, "X-ray Source RS40B1," 2017. [Online]. Available: https://www.prevac.eu/en/2,offer/37,instruments/119,x-ray-source-40b1.html.

(4) Lips, K.; Schulze, T. F.; Starr, D. E.; Bär, M.; Wilks, R. G.; Fenske, F.; Ruske, F.; Reiche, M.; van de Krol, R.; Reichardt, G.; Schäfers, F.; Hendel, S.; Follath, R.; Bahrdt, J.; Peredkov, S.; DeBeer, S.; Hävecker, M.; Knop-Gericke, A.; Rau, B.; Kaufmann, C. A.; Schlatmann, R.; Schlögl, R.; Rech, B.; Raoux, S. EMIL: The Energy Materials in-Situ Laboratory Berlin - a Novel Characterization Facility for Photovoltaic and Energy Materials. In *Proceedings of the 31st European Photovoltaic Solar Energy Conference and Exhibition*, Hamburg, 2015. Munich: WIP, 2015.

(5) Gorgoi, M.; Svensson, S.; Schäfers, F.; Öhrwall, G.; Mertin, M.; Bressler, P.; Karis, O.; Siegbahn, H.; Sandell, A.; Rensmo, H.; Doherty, W.; Jung, C.; Braun, W.; Eberhardt, W. The High Kinetic Energy Photoelectron Spectroscopy Facility at BESSY Progress and First Results. *Nucl. Instrum. Methods Phys. Res., Sect. A* **2009**, *601*, 48–53.

(6) Schaefers, F.; Mertin, M.; Gorgoi, M. KMC-1: A High Resolution and High Flux Soft X-ray Beamline at BESSY. *Rev. Sci. Instrum.* **2007**, *78*, 123102. DOI: 10.1063/1.2808334.

(7) Seah, M. P.; Gilmore, I. S.; Spencer, S. J. XPS : Binding Energy Calibration of Electron Spectrometers 4-Assessment of Effects for Different X-ray Sources, Analyser Resolutions, Angles of Emission and Overall Uncertainties. *Surf. Interface Anal.* **1998**, *26*, 617–641.

(8) [Online], Available: http://home.uni-leipzig.de/unifit/.

(9) De Padova, P.; Fanfoni, M.; Larciprete, R.; Mangiantini, M.; Priori, S.; Perfetti, P. A Synchrotron Radiation Photoemission Study of the Oxidation of Tin. *Surf. Sci.* **1994**, *313*, 379-391. DOI: 10.1016/0039-6028(94)90058-2.

(10) Chastain, J.; King, R. C.; Moulder, J. F. *Handbook of X-ray Photoelectron Spectroscopy: A Reference Book of Standard Spectra for Identification and Interpretation of XPS Data*. Physical Electronics Eden Prairie, MN, 1995.

(11) Kendelewicz, T.; Soukiassian, P.; Bakshi, M. H.; Hurych, Z.; Lindau, I.; Spicer, W. E. Soft X-ray Core Level Photoemission Study of the Cs/InP Interface Formation. *J. Vac. Sci. Technol., B: Microelectron. Process. Phenom.* **1988**, *6*, 1331–1335.

(12) Trzhaskovskaya, M.B.; Nefedov, V.I.; Yarzhemsky, V.G. Photoelectron Angular Distribution Parameters for Elements Z=1 to Z=54 in the Photoelectron Energy Range 100–5000 eV. *At. Data Nucl. Data Tables* **2001**, *77*, 97-159.

(13) Trzhaskovskaya, M.B.; Nefedov, V.I.; Yarzhemsky, V.G. Photoelectron Angular Distribution Parameters for Elements Z=55 to Z=100 in the Photoelectron Energy Range 100–5000 eV. *At. Data Nucl. Data Tables* **2002**, *82*, 257-311.

(14) Kratos Analytical Internal Data.

(15) Wagner, C. D.; Davis, L. E.; Zeller, M. V.; Taylor, J. A.; Raymond, R. H.; Gale, L.H. Empirical Atomic Sensitivity Factors for Quantitative Analysis by Electron Spectroscopy for Chemical Analysis. *Surf. Interface Anal.* **1981**, *3*, 211.

(16) Briggs, D.; Seah, M. P. *Practical Surface Analysis*; 2nd ed.; John Wiley& Sons: New York, 1990; Vol. 1.

(17) Tanuma, S.; Powell, C. J.; Penn, D. R. Calculations of Electron Inelastic Mean Free Paths for 31 Materials. *Surf. Interface Anal.* 1**988**; *11*, 577.

(18) Tanuma, S.; Powell, C. J.; Penn, D. R. Calculations of Electron Inelastic Mean Free Paths. II. Data for 27 Elements over the 50–2000 eV Range. *Surf. Interface Anal.* **1991**; *17*, 911.

(19) Powell, C. J., Jablonski, A. Evaluation of Calculated and Measured Electron Inelastic Mean Free Paths Near Solid Surfaces. *J. Phys. Chem. Ref. Data* **1999**; *28*, 19.

(20) National Institute of Standards and Technology, "NIST X-ray Photoelectron Spectroscopy (XPS) Database." [Online], Available: http://srdata.nist.gov/xps/Default.aspx.

(21) Chung, I.; Song, J. H.; Im, J.; Androulakis, J.; Malliakas, C. D.; Li, H.; Freeman, A. J.; Kenney, J. T.; Kanatzidis, M. G. $CsSnI_3$: Semiconductor or Metal? High Electrical Conductivity and Strong Near-Infrared Photoluminescence from a Single Material. High Hole Mobility and Phase-Transitions. *J. Am. Chem. Soc.* **2012**, *134*, 8579−8587. DOI: 10.1021/ja301539s.

(22) Jung, M. C.; Raga, S. R.; Qi, Y. Properties and Solar Cell Applications of Pb-Free Perovskite Films Formed by Vapor Deposition. *RSC Adv.* **2016**, *6*, 2819–2825. DOI: 10.1039/c5ra21291j.

(23) Spicer, W. E.; Lindau, I.; Su, C. Y.; Chye, P. W.; Pianetta, P. Core-level Photoemission of the Cs-O Adlayer of NEA GaAs Cathodes. *Appl. Phys. Lett.* **1978**, *33*, 934.

(24) Hrbek, J.; Yang, Y.W.; Rodriguez, J.A. Oxidation of Cesium Multilayers. *Surf. Sci.* **1993**, *296*, 164-170.

(25) Hu, Y.; Wang, Q.; Shi. Y.-L.; Li, M.; Zhang, L.; Wang, Z.-K.; Liao, L.-S. Vacuum-Evaporated All-Inorganic Cesium Lead Bromine Perovskites for High-Performance Light-Emitting Diodes. *J. Mater. Chem. C* **2017**, *5*, 8144-8149.

(26) Scanlon, D. O.; Dunnill, C. W.; Buckeridge, J.; Shevlin, S. A.; Logsdail, A. J.; Woodley, S. M.; Catlow, C. R. A.; Powell, M. J.; Palgrave, R. G.; Parkin, I. P.; Watson, G. W.; Keal, T. W.; Sherwood, P.; Walsh, A.; Sokol, A. A. Band Alignment of Rutile and Anatase TiO_2. *Nat. Mater.* **2013**, *12*, 798–801.

(27) Zheng, J.-C.; Huan, C. H. A.; Wee, A. T. S.; Kuok, M. H. Electronic Properties of $CsSnBr_3$: Studies by Experiment and Theory. *Surf. Interface Anal.* **1999**, *28*, 81–83.

(28) Themlin, J.-M.; Chtaïb, M.; Henrard, L.; Lambin, P.; Darville, J.; Gilles, J.-M. Characterization of Tin Oxides by X-ray-Photoemission Spectroscopy. *Phys. Rev. B* **1992**, *46*, 2460–2466.

(29) Endres, J.; Egger, D. A.; Kulbak, M.; Kerner, R. A.; Zhao, L.; Silver, S. H.; Hodes, G.; Rand, B. P.; Cahen, D.; Kronik, L.; Kahn, A. Valence and Conduction Band Densities of States of Metal Halide Perovskites: A Combined Experimental–Theoretical Study. *J. Phys. Chem. Lett.* **2016**, *7*, 2722-2729. DOI: 10.1021/acs.jpclett.6b00946.

(30) Mao, X.; Sun, L.; Wu, T.; Chu, T.; Deng, W.; Han, K. First-Principles Screening of All-Inorganic Lead-Free ABX3 Perovskites. *J. Phys. Chem. C* **2018**, *122,* 7670-7675. DOI: 10.1021/acs.jpcc.8b02448.